

CHAPTER-4

Results of Experimental Techniques

This chapter contains the results and discussion of the characterizations performed on the blend electrolyte samples.

INTRODUCTION

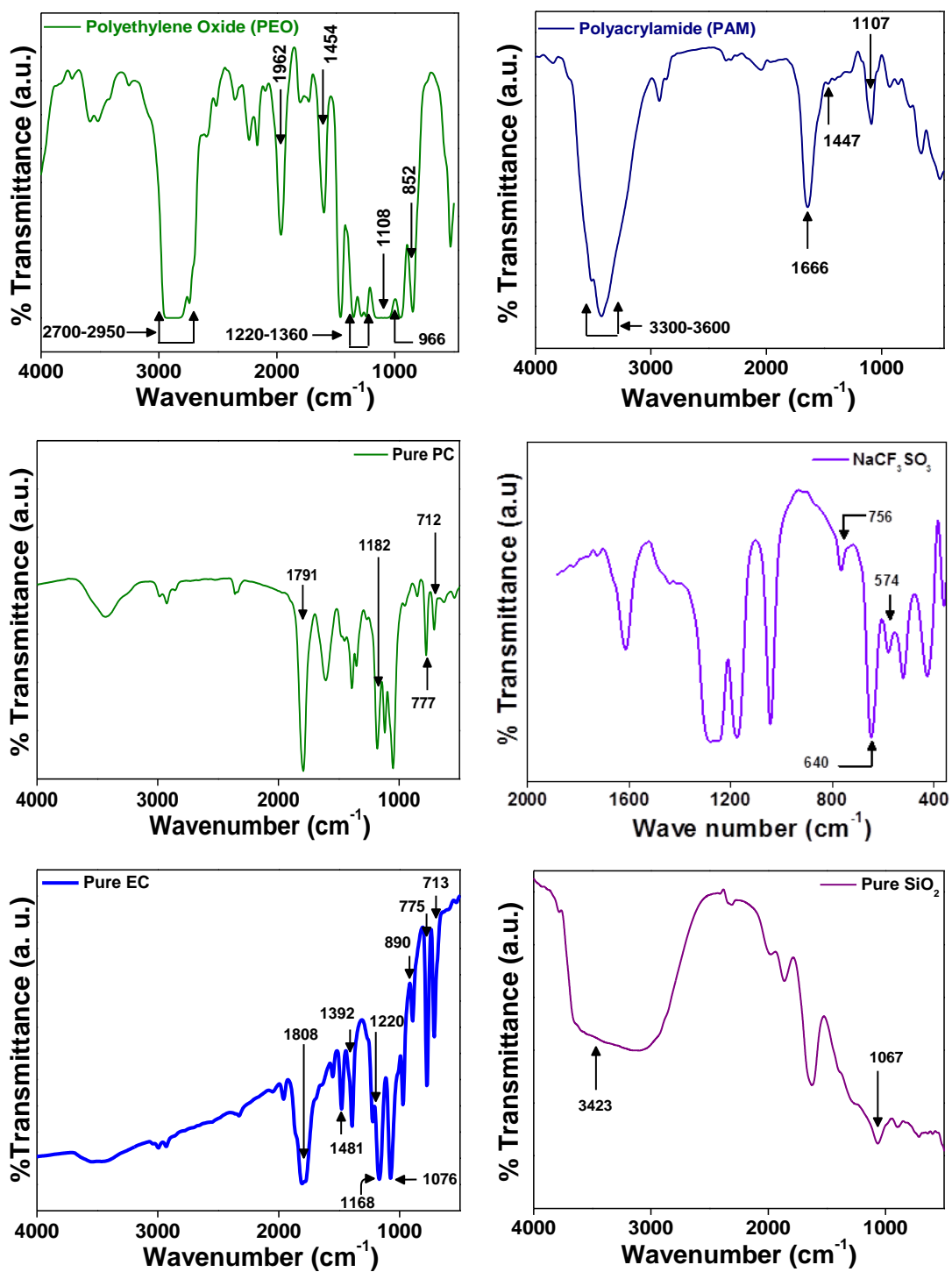
This chapter presents the results of the characterizations carried out for the synthesized polymer blend electrolytes, plasticized blend electrolytes and plasticized polymer blend nano-composites. Characterization results help us to study the structural, morphological and thermal changes in the properties of the electrolyte systems and also backup our analysis of the results obtained for impedance and transport properties of the materials.

4.1 FT-IR Studies

Vibrational spectroscopy is a potentially useful tool for structural analysis and in deriving conformational variations (*Pielichowska et al., 2008*). Figs. 4.1(a-f) show IR spectra of the starting materials namely the polymers Polyethylene Oxide (PEO) and Polyacrylamide (PAM), Sodium trifluoromethanesulfonate (NaCF_3SO_3) salt, plasticizers ethylene carbonate (EC) and propylene carbonate (PC). Their peak positions and the corresponding assignments are given in table 4.1.

Table 4.1 Peak positions and assignments of IR spectra of all the starting materials.

Material	Peak Positions (cm ⁻¹)	Peak Assignments	References
Polyethylene Oxide (PEO)	852	C-C symmetric stretching	<i>Mohan et al., 2006</i>
	966	CH ₂ rocking	<i>Mohan et al., 2006; Sharma, 2013</i>
	1220-1360	CH ₂ twisting and wagging	
	1454	CH ₂ scissoring	
	2700-2950	symmetric and asymmetric C-H stretching modes of CH ₂	
Polyacrylamide (PAM)	1666	Stretching vibration of – C=O	<i>Asgharzadehahmadi et al., 2012</i>
	3300-3600	NH ₂ stretching vibrations	
Sodium Triflate (NaCF₃SO₃)	574	$\delta_a(\text{CF}_3)$	<i>Kumar and Hashmi, 2010; Pandey and Hashmi, 2009</i>
	690	$\delta_a(\text{SO}_3)$	
	756	$\delta_s(\text{CF}_3)$	
Ethylene Carbonate (EC)	713	Ring bending	<i>Sharma, 2013; Winie and Arof, 2006; Matsushita et al., 2005; Akita et al., 2013</i>
	775	CH ₂ rocking	
	890	Ring breathing	
	1076		
	1168	C-O-C symmetric stretching	
	1392	CH ₂ wagging	
	1481	CH ₂ bending	
	1808	C=O stretching	
Propylene Carbonate (PC)	712	Symmetric ring deformation	<i>Kumar, 2010</i>
	777	Ring breathing	<i>Rajendran and Prabhu, 2009</i>
	1791	C=O stretching	
Silicon dioxide (SiO₂)	1067	Si-O-Si asymmetric peak	<i>Ketabi and Lian, 2013</i>
	3423	O-H stretching of surface hydroxyl group	<i>Ramesh and Wen, 2009</i>



Figs. 4.1(a-f) IR-spectra of all the starting materials.

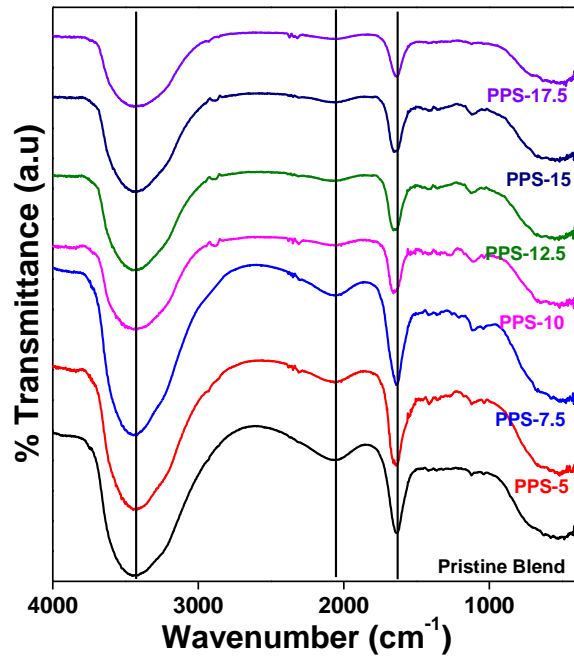


Fig. 4.2 IR-spectra of pristine blend and PPS-system.

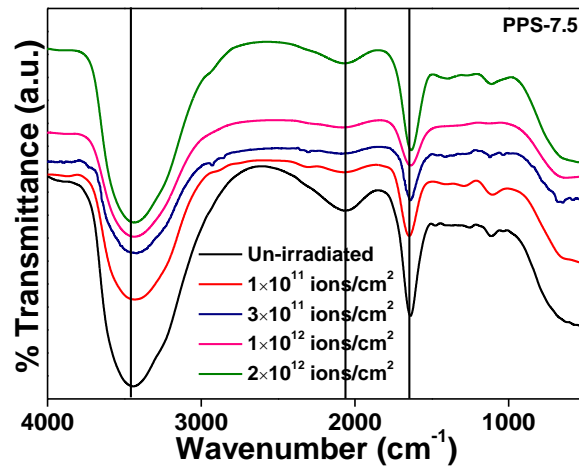


Fig. 4.3 IR-spectra of irradiated PPS-7.5 sample.

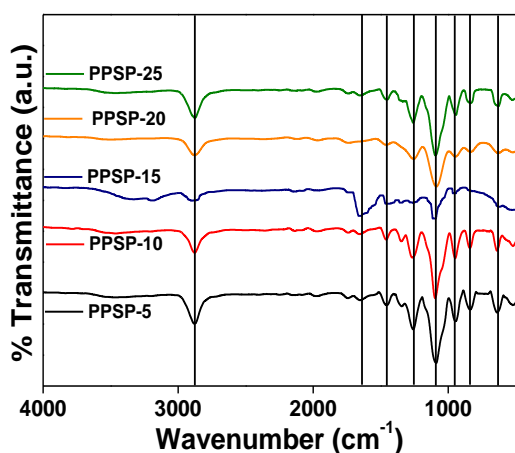


Fig. 4.4 IR-spectra of PPSP-system.

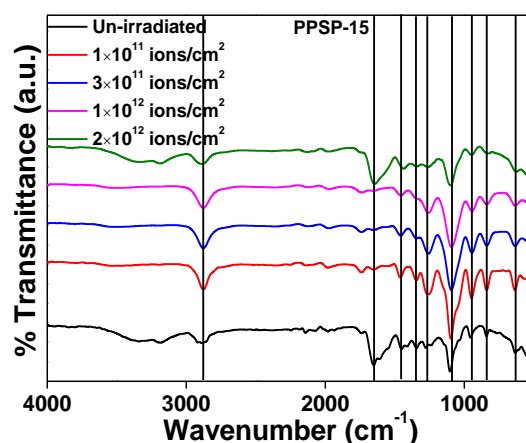


Fig. 4.5 IR-spectra of irradiated PPSP-15 sample.

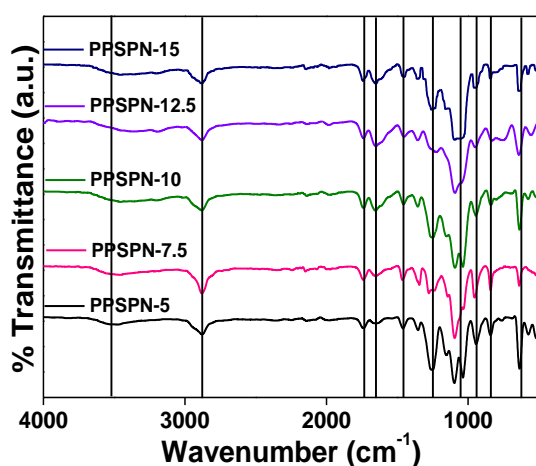


Fig. 4.6 IR-spectra of PPSPN-system.

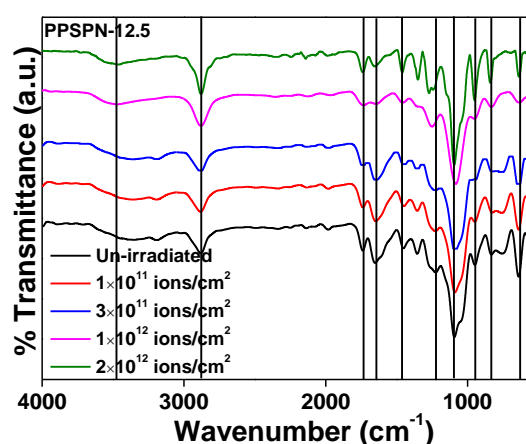


Fig. 4.7 IR-spectra of irradiated PPSPN-12.5 sample.

The IR spectra of the materials also provide the information about the occurrence of complexation also between various constituents (Ramesh et al., 2007). Fig. 4.2 shows IR spectra of PPS system. All the samples show only two peaks (1633 cm^{-1} and 2059 cm^{-1}) and a broad halo at 3440 cm^{-1} . Peak at 1633 cm^{-1} corresponds to the -C=O stretching vibration mode of PAM which shifted from 1666 cm^{-1} . Slight dip like peak at 2059 cm^{-1} may be due to the combination of the peaks observed for PEO in the range of 1601 cm^{-1} - 2240 cm^{-1} and the broad halo structure at 3433 cm^{-1} is NH_2 stretching vibration of PAM which formed a broad region between 3300 cm^{-1} - 3600 cm^{-1} in pure PAM. All other peaks observed for PEO are suppressed and also no peaks corresponding to the triflate salt are observed. This suppression of peaks, slight shifting of the wave-numbers and absence of most of the peaks observed in parent materials point out a good miscibility of the polymers and polymer/salt complexation (Ramesh

et al., 2007). It is also observed that with increase in salt concentration there is a decrease in the intensity of the peaks and the peaks shift towards higher wave number side. PPS-17.5 sample shows least intense peaks among all other samples which points out that it is the more amorphous than the others. Shifting of the peak position towards higher wave number indicates the decrease in bond length of the group in a polymer chain.

PPS-17.5 sample was irradiated at different fluences by 80 MeV swift heavy O^{6+} ion beam carried out using material science beam line facility of pelletron accelerator at IUAC, New Delhi. Fig. 4.3 shows FT-IR spectra of PPS-17.5 sample irradiated at various fluences. With increase in fluence from 1×10^{11} ions/cm² to 2×10^{12} ions/cm², only slight decrease in intensity of the peaks and minor shift towards higher wave-number side is observed. No extra peaks occur post irradiation. Irradiation degrades the polymer and breaking down of polymer chains results in changes in bond length and crystallinity which are manifested in the form of shifting of peaks and lowering of the intensity. These trivial changes observed in the IR-spectra of BPE samples, suggest that the irradiation caused, structural rearrangements, changes in bonds and isomerization (*Kumar et al.*, 2010a, 2010b) in the electrolyte system but did not lead to a complete wipe-out of the overall structure of the polymer host matrix.

IR spectra of EC+PC plasticized blend electrolytes are shown in Fig. 4.4. The peak observed at 637 cm^{-1} is contributed by $\delta_a(SO_3)$, free triflate anions in sodium triflate salt (*Kumar and Hashmi*, 2010; *Pandey and Hashmi*, 2009). Although this peak was not apparent for any sample of PPS system, here it is clearly observed to decrease with increase in EC+PC content. The peak shows minimum at PPSP-15 sample and then resurfaces slightly at PPSP-20 and 25 samples. Peak observed at 844 cm^{-1} is contributed from C-C symmetric stretching mode of pure PEO observed at 852 cm^{-1} in pure PEO. 952 cm^{-1} peak is the contribution of CH_2 rocking mode of PEO observed at 966 cm^{-1} in pure PEO. Peak observed at 1089 cm^{-1} has a typical shape, a dip with a small step (Fig. 4.4) which suggests that it is the combination of peaks corresponding to ring breathing modes of pure EC observed at 890 cm^{-1} and 1076 cm^{-1} . 1254 cm^{-1} peak is again due to combination of two peaks namely 1168 cm^{-1} and 1392 cm^{-1} corresponding respectively to C-O-C symmetric stretching and CH_2 wagging modes of pure EC. Peak observed at 1462 cm^{-1} corresponds to CH_2 bending mode of EC shifted from 1481 cm^{-1} . An

unassigned peak at 2878 cm^{-1} is observed throughout the system. In each of the above case we see that the peaks broaden with increase in EC+PC content, shows minimum at PPSP-15 sample and resurface at PPSP-20 and 25 samples with more sharp features for PPS-25 sample as compared to PPSP-20 sample. Also we observe a flat region between 1462 cm^{-1} - 2878 cm^{-1} where the region from 1462 cm^{-1} - 1820 cm^{-1} is particularly uneven. This uneven region is interpreted as the consequence of overlapping of three vibrations namely 1481 cm^{-1} - CH_2 bending mode of EC, 1808 cm^{-1} - $\text{C}=\text{O}$ stretching mode of EC and 1791 cm^{-1} - $\text{C}=\text{O}$ stretching mode of PC. All the above observations clearly point out that there is an excellent miscibility of the plasticizers with the blend electrolyte system.

IR spectra of PPSP-15 sample irradiated at various fluences are shown in Fig. 4.5. After irradiation all the peaks shift towards low wavenumber side with increase in fluence up to critical fluence value ($1 \times 10^{12}\text{ ions/cm}^2$). Beyond it ($2 \times 10^{12}\text{ ions/cm}^2$), the peaks become sharp and also shift slightly towards higher wavenumber side. Irradiation itself did not give rise to any new peak, but the peak observed at 1392 cm^{-1} observed in pure EC due to CH_2 wagging mode resurges. This peak also shows decrease in intensity up to critical fluence and increase thereafter. These observations lead us to conclude that the sample is most amorphous at critical fluence value and re-crystallization takes place at $2 \times 10^{12}\text{ ions/cm}^2$ fluence.

Fig. 4.6 shows IR analysis of PPSPN system. $\delta_a(\text{SO}_3)$ peak observed at 690 cm^{-1} for free triflate anions is shifted to 628 cm^{-1} in PPSPN system. Peak observed at 840 cm^{-1} is contributed by, C-C symmetric stretching mode of pure PEO (852 cm^{-1}). Peak at 933 cm^{-1} is due CH_2 rocking mode of PEO (966 cm^{-1}). Peak observed at 1053 cm^{-1} is split into two for PPSPN-5 and PPSPN-10 samples and shows a dip with a small step for PPSPN-7.5, 12.5 and 15 samples. This peak is due to combination of three peaks namely, the peaks corresponding to ring breathing modes of pure EC observed at 890 cm^{-1} and 1076 cm^{-1} and the peak at 1067 cm^{-1} depicting Si-O-Si asymmetric peak of SiO_2 . The peak observed at 1248 cm^{-1} is contribution of two peaks of EC namely 1168 cm^{-1} corresponding to C-O-C symmetric stretching and 1392 cm^{-1} CH_2 wagging modes of pure EC. Peak at 1462 cm^{-1} is again contributed by EC (CH_2 bending mode of EC) and the 1656 cm^{-1} peak is observed due to the stretching vibration of $-\text{C}=\text{O}$ of PAM. Peak observed at 1739 cm^{-1} is contribution of $-\text{C}=\text{O}$ stretching mode of PC. The long

region with an uneven stretch as observed in case of PPSP system is observed in PPSPN system between 1739 cm^{-1} - 2878 cm^{-1} . A small dip at 3521 cm^{-1} is observed in the PPSPN system corresponding to -O-H stretching of surface hydroxyl group of SiO_2 shifted from 3423 cm^{-1} . The peak intensities are observed to be low for PPSPSN-5 and 7.5 samples and the peaks shift toward low wavenumber side. For PPSPSN-10 sample, the peak intensity increases slightly and the peaks shift towards high wave-number side. For PPSPSN-12.5 sample, the peak intensities decrease o minimum and the peaks shift towards low wavenumbers and for PPSPSN-15 sample, the intensity increases again and the peaks shift towards high wavenumber. From the above observations we conclude that PPSPSN-12.5 sample is more amorphous in nature as compared to the others.

IR-spectra of PPSPN-12.5 sample irradiated at various fluences is plotted in [Fig. 4.7](#). All the observed peaks shift towards low wave-number side after irradiation and their intensities also decrease up to the value of critical fluence, further irradiation shows more intense and sharp peaks. This shifting towards lower wave number side is indicative of increase in bond lengths after irradiation and structure is opening with increase in volume.

4.2 XRD Analysis

X-ray diffractograms of the pristine polymers PEO, PAM and their blend are presented in [Fig. 4.8](#). PAM shows only a broad hump at $2\theta = 25^\circ$ indicating its amorphous nature. PEO shows crystalline peaks at $2\theta = 19^\circ$ and 23° originating due to the orderings of poly ether side chains ([Ketabi and Lian, 2013](#); [Sharma, 2013](#)). In the blend sample without salt, characteristic peaks of PEO at $2\theta = 19^\circ$ and 23° are observed. However, intensity of the peak at $2\theta = 19^\circ$ has reduced and the peak at $2\theta = 23^\circ$ has split up.

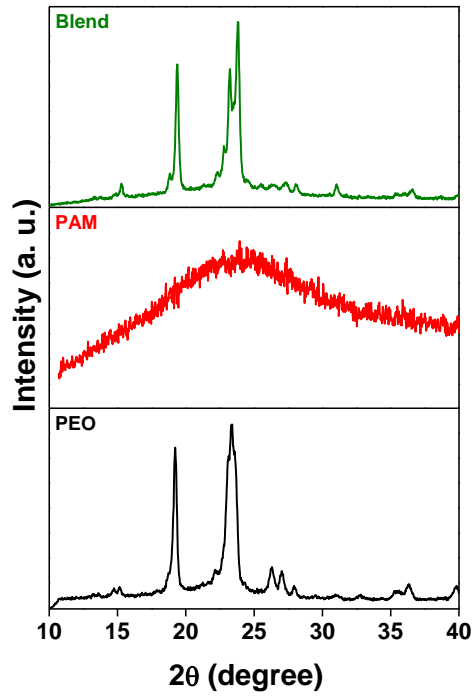


Fig. 4.8 X-ray diffractograms of polymers and pristine blend.

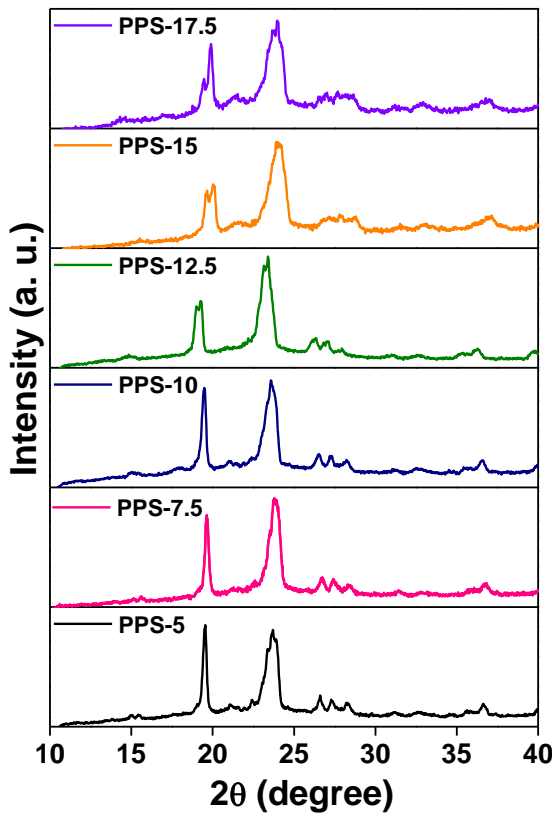


Fig. 4.9 X-ray diffractograms of PPS-system.

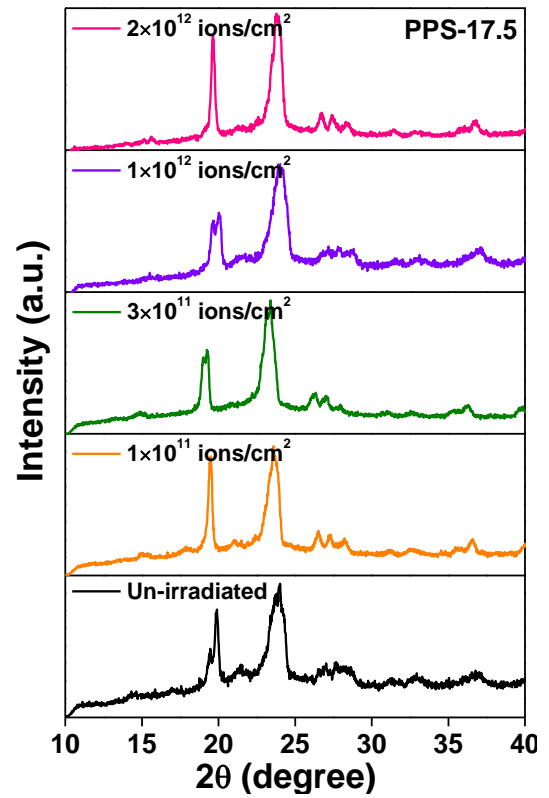


Fig. 4.10 X-ray diffractograms of irradiated PPS-17.5 sample.

Fig. 4.9 shows diffractograms of blend electrolyte samples with varying concentrations of NaCF₃SO₃. In each diffractogram we observe peaks at $2\theta = 19^\circ$ and $2\theta = 23^\circ$. The intensities of the peaks show continuous decrease from PPS-5 to PPS-17.5 sample. The peaks observed for PPS-17.5 sample are diminished and have lowest intensity. Peaks corresponding to NaCF₃SO₃ are not observed in the electrolyte samples which ascertain that the salt does not remain as an individual entity in the system (Dave and Kanchan, 2018). Overall changes in the diffractogram patterns of pristine components, suppression of certain peaks, decrease in intensities and non-occurrence of salt peaks in the electrolyte system suggest complete dissociation of salt in the system and the resulting in a good polymer-polymer and polymer-salt complexation (Pradeepa et al., 2015).

To see the effect of irradiation on the structure, the diffractograms of PPS-17.5 sample irradiated at different fluences are shown in Fig. 4.10. However after irradiation with fluence of 1×10^{11} ions/cm² (Fig. 4.10) the peak intensities increase, which suggest the increase in the degree of crystallinity. We observe that the intensity of the peak observed at $2\theta = 19^\circ$ decreases with increasing fluence up to 3×10^{11} ions/cm². At 1×10^{12} ions/cm² fluence, the peak splits a little and has lowest intensity among all the irradiated samples. But at 2×10^{12} ions/cm² fluence, the intensity of both peaks increases. According to R. Percolla et al, for pure PVDF polymer the degree of crystallinity, in general, increases after low fluence ion irradiation and decreases after high fluence ion irradiation. But in PPS system, after low fluence ion irradiation ($\leq 10^{11}$) crystallinity decreases due to breaking of bonds, which amorphizes the sample. At lower fluences, chain scissioning process is the major reason of decrease in crystallinity of the of the electrolyte materials. But at higher fluence of 2×10^{12} ions/cm², reordering, chain-folding and cross-linking of bonds take place, which form the new crystalline region in the polymer electrolyte (Kumar et al., 2010a).

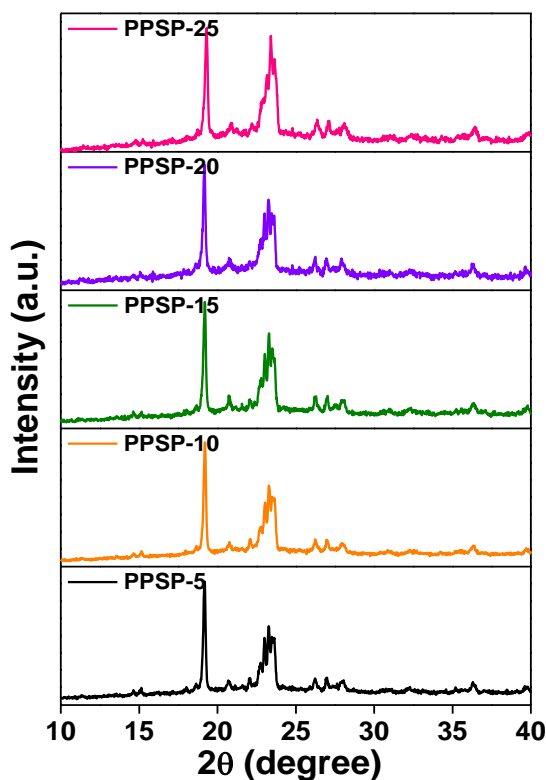


Fig. 4.11 X-ray diffractograms of PPSP-system.

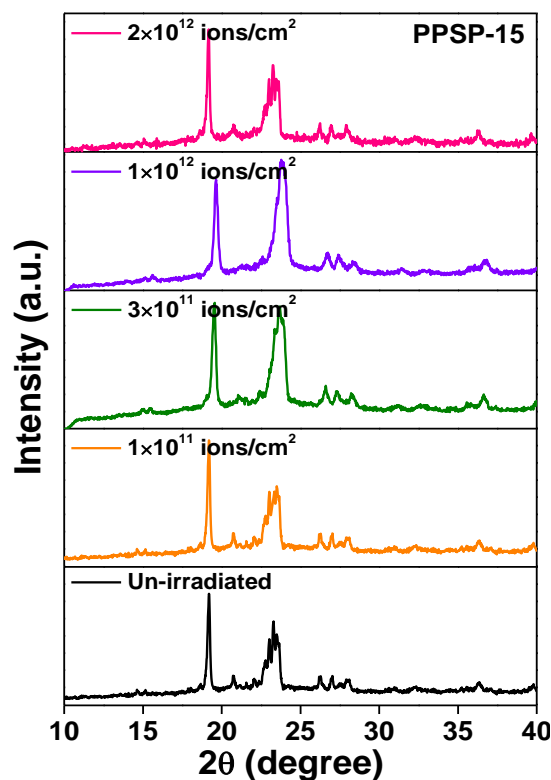


Fig. 4.12 X-ray diffractograms of irradiated PPSP-15 sample.

Fig. 4.11 shows diffractograms for BPE samples with varying EC+PC content. In case of plasticized samples also, two prominent peaks at $2\theta = 19^\circ$ and $2\theta = 23^\circ$ are observed. We do not observe any new peaks which would mark the presence of the plasticizers in the system. This suggests that the plasticizers have amalgamated well with the blend electrolyte system. The intensity of the peak at $2\theta = 19^\circ$ remains unchanged throughout the whole system and only small changes in the $2\theta = 23^\circ$ peak intensity are observed. The intensity of the peak is low for PPSP-5 and 10 samples, becomes minimum at PPSP-15 sample and then shows a slight increase for PPSP-20 and 25 samples. Peak intensity for PPSP-25 sample is marginally high than that of PPSP-20 sample. Broadening of the peaks and decrease in intensity show increase in amorphous nature of the system (Anbazhakan et al., 2017).

Diffractograms of PPSP-15 sample irradiated at various fluences are shown in Fig. 4.12. There are no notable changes in any of the peaks. Only the intensity of the peak at 2θ

$= 23^\circ$ decreases and it broadens slightly with increase in fluence, shows broadest peak at 1×10^{12} ions/cm² fluence and again becomes sharp at 2×10^{12} ions/cm² fluence.

Diffractograms for plasticized blend electrolyte system with varying concentration of nano-SiO₂ particles are presented in Fig. 4.13. For nano dispersed samples also, there are no notable changes in the peak at $2\theta = 19^\circ$. The peak at $2\theta = 23^\circ$ has low intensity at PPSPN-5 and 7.5 samples, increases for PPSPN-10 sample, decreases to become lowest for PPSPN-12.5 sample and again increases for PPSPN-15 sample. With addition of SiO₂, intensity of the crystalline peak decreases and it becomes broader. The increase in broadness of the peak increases the path ways for cation migration.

Fig. 4.14 shows diffractograms of PPSPN-12.5 sample irradiated at various fluences. The intensity of the peak at $2\theta = 19^\circ$ again remains almost unchanged. Only the peak at $2\theta = 23^\circ$ broadens with irradiation up to 1×10^{12} ions/cm² fluence and then becomes sharp at 2×10^{12} ions/cm² fluence.

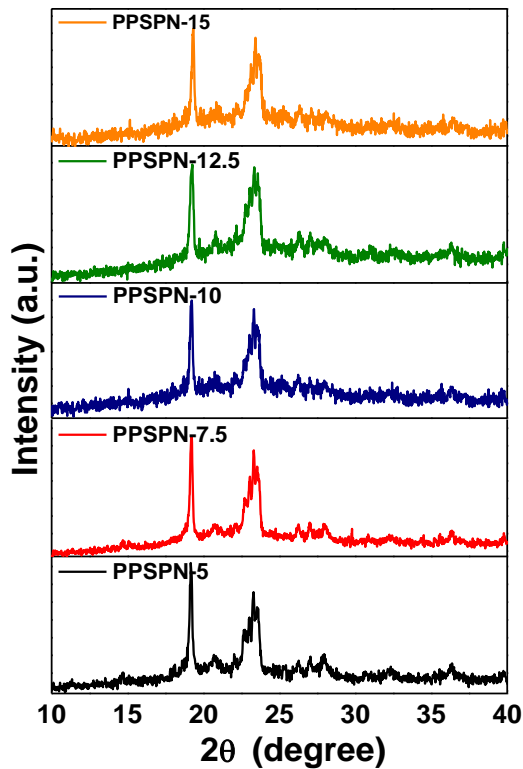


Fig. 4.13 X-ray diffractograms of PPSPN-system.

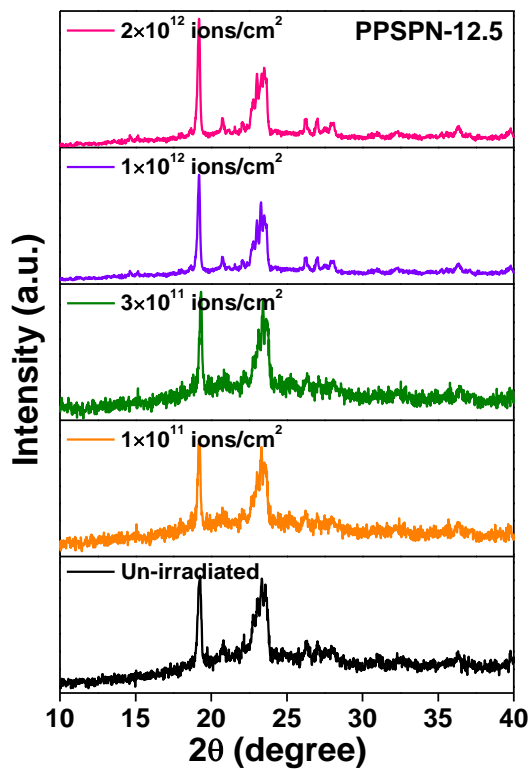


Fig. 4.14 X-ray diffractograms of irradiated PPSPN-12.5 sample.

4.3 Thermal Properties

Differential Scanning Calorimetry is a thermodynamic technique in which the difference in the amount of heat required to increase or decrease the temperature of a sample and reference is measured as a function of temperature. Melting temperature is characteristic of phase transition phenomenon occurring in a crystalline polymer or in crystalline portion of a semi-crystalline polymer (*Choudhary and Sengwa, 2017*). PAM being an amorphous polymer does not show typical endothermic melting peak and so we have interpreted thermal properties of the prepared blend polymer electrolyte systems based on the melting temperature of PEO. In the figures below, all blend samples show single endothermic peak in the temperature range 68 °C-53 °C. This temperature range is in the neighbourhood of the melting temperature of pure PEO polymer (65 °C, *Morreno et al., 2014*).

Fig. 4.15(a) shows DSC plots of the BPE samples. With the addition of NaCF₃SO₃, we see that the melting temperature decreases monotonically, and PPS-17.5 sample shows minimum T_m (59 °C). The slight shift of melting temperature T_m and decrease in intensity of endothermic peak is a clear indication of changes in crystallinity or localized influence of polymer chains conformation (*Ramesh et al., 2011*). Crystallinity reduction with salt addition in polymer electrolytes is a typical and largely discussed behavior (*Borges et al., 2011; Armand, 1994; Chiu et al., 2005*). To highlight the changes in the melting temperature with salt concentration, we plot melting temperature as a function of salt concentration as in **Fig. 4.15(b)**.

Melting temperatures of PPS-17.5 sample after irradiation at various fluences is plotted in **Fig. 4.16(a)**. After irradiation also, the sample shows single endothermic peak. Melting temperature of irradiated sample decreases up to the value of critical fluence (1×10^{12} ions/cm², (56 °C)) and then increases at 2×10^{12} ions/cm² fluence again, this observation is more pronounced in **Fig. 4.16(b)** which shows the trend in T_m as a function of fluence.

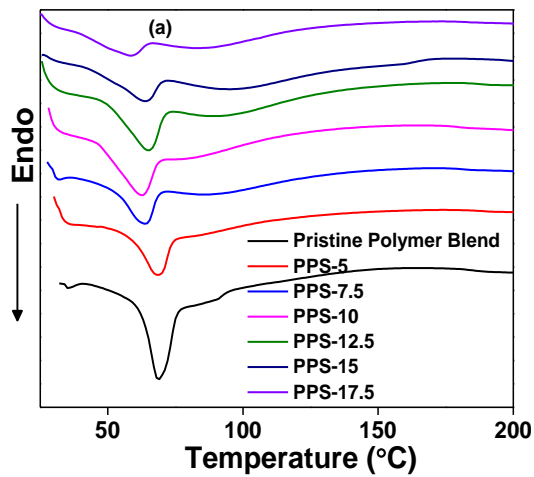


Fig. 4.15(a) DSC thermograms of PPS-system.

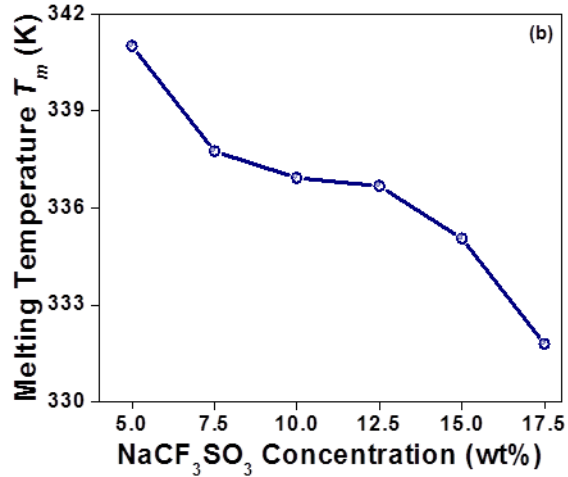


Fig. 4.15(b) Melting temperature (T_m) as a function of salt concentration.

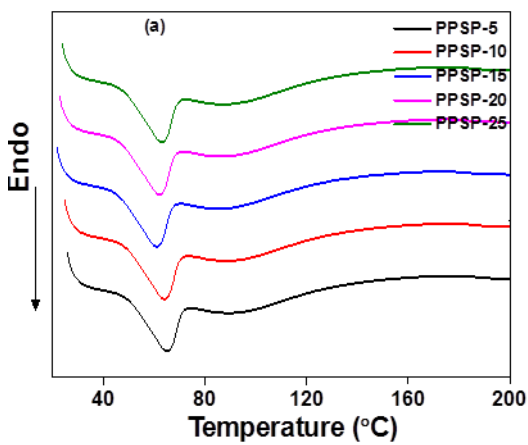


Fig. 4.16(a) DSC thermograms of irradiated PPS-17.5 sample.

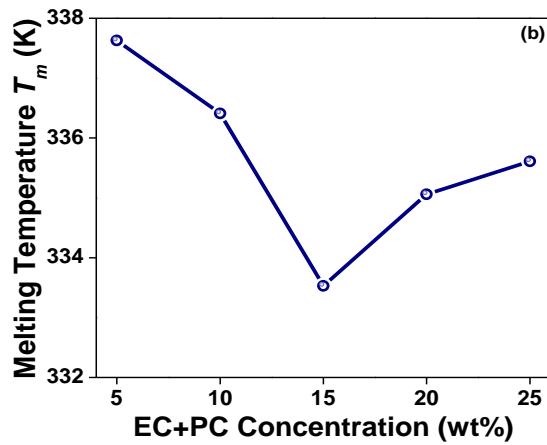


Fig. 4.16(b) Melting temperature (T_m) as a function of fluence for irradiated PPS-17.5 sample.

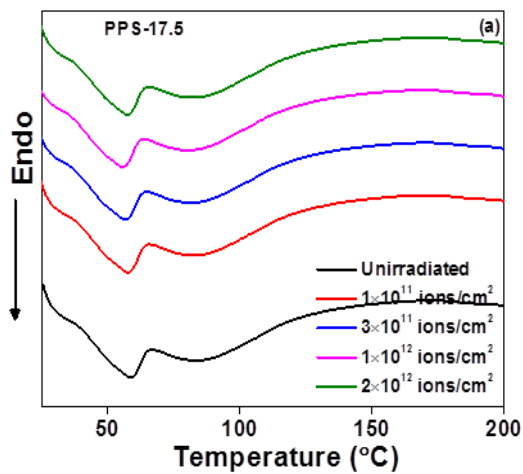


Fig. 4.17(a) DSC thermograms of PPSP-system.

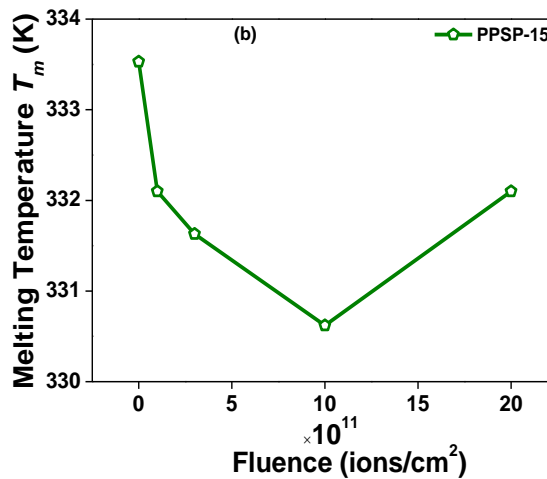


Fig. 4.17(b) Melting temperature (T_m) as a function of EC+PC concentration.

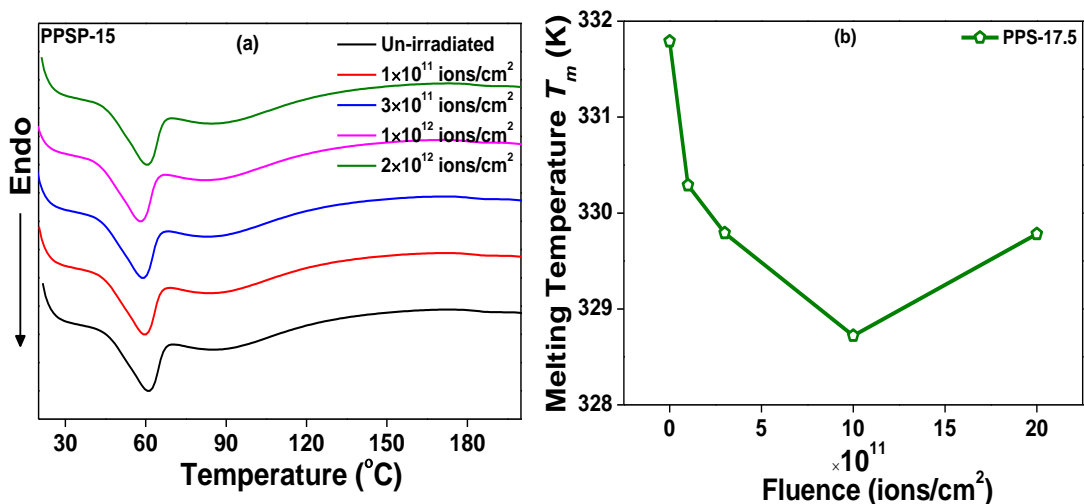


Fig. 4.18(a) DSC thermograms of irradiated PPSP-15 sample.

Fig. 4.18(b) Melting temperature (T_m) as a function of fluence for irradiated PPSP-15 sample.

DSC thermograms of plasticized blend electrolyte samples are plotted in Fig. 4.17(a). The melting temperatures decrease with increase in addition of EC+PC up to PPSP-15 sample (61 °C) and then increase for PPSP-20 and 25 samples. Fig. 4.17(b) showing the trend of T_m as a function of EC+PC content projects the fact that the T_m shows a minimum for PPSP-15 sample.

Fig. 4.18(a) shows DSC thermograms of irradiated PPSP-15 sample and the trend in T_m as a function of fluence is plotted in Fig. 4.18(b). It is clearly observed that the T_m decreases up to value of critical fluence (58 °C) and then increases at further fluence.

Fig. 4.19(a) shows the DSC thermograms of plasticized blend electrolyte system with varying concentrations of SiO₂. Addition of SiO₂ leads to a decrease in the value of T_m for PPSPN-5 and PPSPN-7.5 sample. For PPSPN-10 sample, T_m increases slightly. At PPSPN-12.5 sample, T_m drops to minimum (57 °C) and then again increases for PPSPN-15 sample. Also, the peaks broaden and follow the suit of the melting temperature values. The zigzag trend observed in T_m values with SiO₂ addition is well interpreted from the plot of T_m vs SiO₂ concentration as in Fig. 4.19(b). Choudhary and Sengwa (2017) explain the broadening of the endothermic peaks to be due to the formation of weak nucleation sites as a consequence of addition of nano SiO₂.

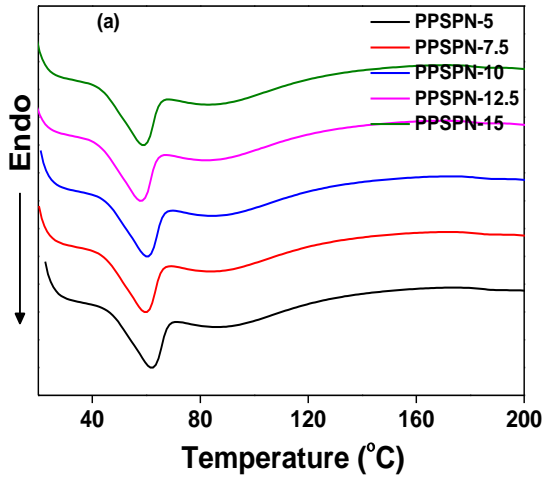


Fig. 4.19(a) DSC thermograms of PPSPN-system.

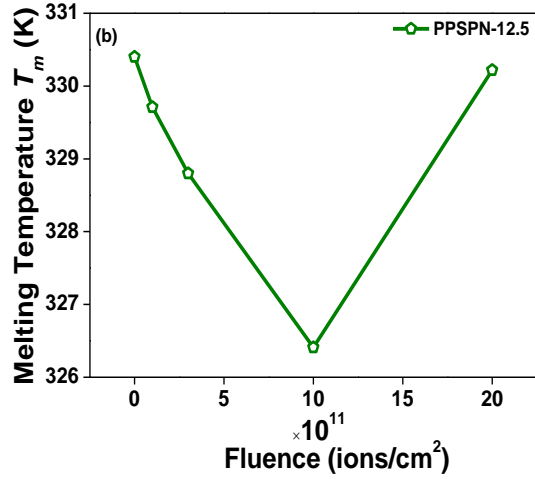


Fig. 4.19(b) Melting temperature (T_m) as a function of SiO_2 concentration.

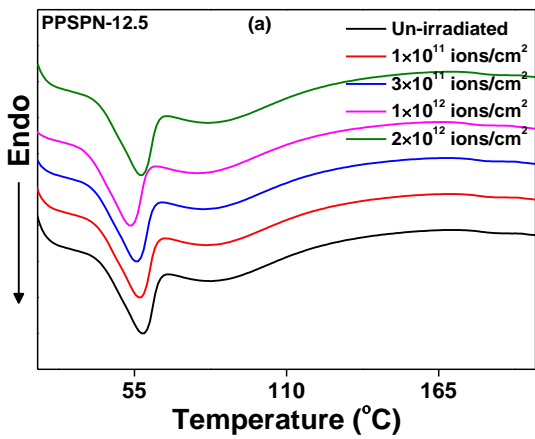


Fig. 4.20(a) DSC thermograms of irradiated PPSPN-12.5 sample.

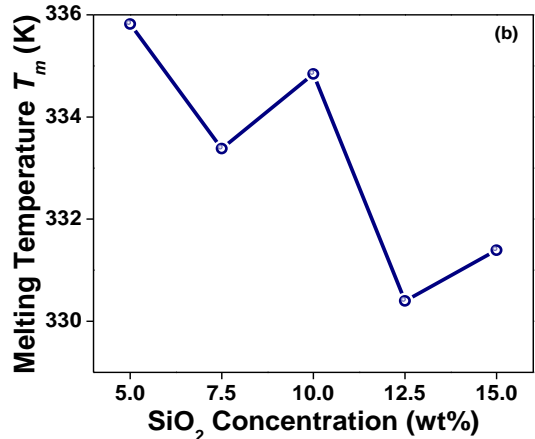


Fig. 4.20(b) Melting temperature (T_m) as a function of fluence for irradiated PPSPN-12.5 sample.

Fig. 4.20(a) presents DSC thermograms of PPSPN-12.5 sample irradiated at different fluences and the trend observed for T_m as a function of fluence is plotted in Fig.

4.20(b). It is apparent that the T_m values decrease with fluence up to 1×10^{12} ions/cm² (53 °C) and then increase at higher fluence.

A common characteristic that is linked with all the thermograms is that with decrease in T_m values, the endothermic peaks broaden and then become sharp when the T_m values increase.

4.4 SEM Studies

Scanning Electron Microscopy is a technique which produces images of a sample by scanning it with a focused beam of electrons. The electrons interact with the atoms in the sample, producing various signals that can be detected and contain information about the surface topography and composition of the sample.

Figs. 4.21(a-d) show SEM micrographs of PPS-17.5 sample before irradiation and after irradiation at three different fluences. SEM image of the sample before irradiation shows a rough morphology with no remarkable sharp features. When polymers are exposed to SHI irradiation, stiff chains of the polymers undergo scissioning due to its degradation. These broken chains form disordered pore-like structures with voids in between them are observed. At lower fluences (1×10^{12} ions/cm²), chain scissioning process dominates and very prominent pore structures are observed. At higher fluence (2×10^{12} ions/cm²), large number of shattered chains recombine to form a rigid cross-linked network and an apparent decrease in the pore structures is noted. **Seki et al. (2012)** also observed significant surface modifications in the microstructure of carbon nano-fibres post ion beam irradiation.

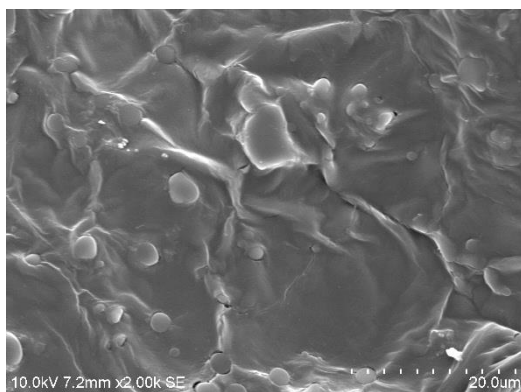


Fig. 4.21(a) SEM micrograph of un-irradiated PPS-17.5 sample.

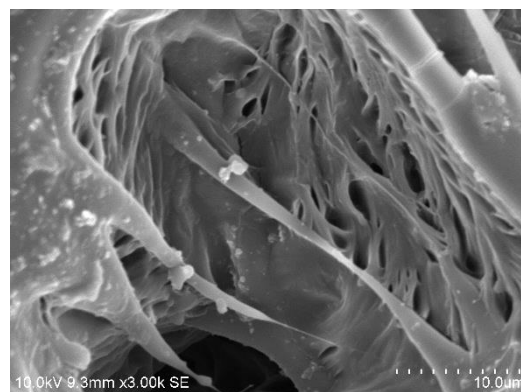


Fig. 4.21(b) SEM micrograph of PPS-17.5 sample irradiated at 1×10^{11} ions/cm² fluence.



Fig. 4.21(c) SEM micrograph of PPS-17.5 sample irradiated at 1×10^{12} ions/cm² fluence.



Fig. 4.21(d) SEM micrograph of PPS-17.5 sample irradiated at 2×10^{12} ions/cm² fluence

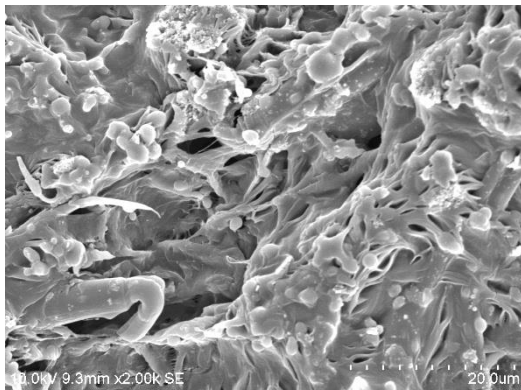


Fig. 4.22(a) SEM micrograph of un-irradiated PPSP-15 sample.

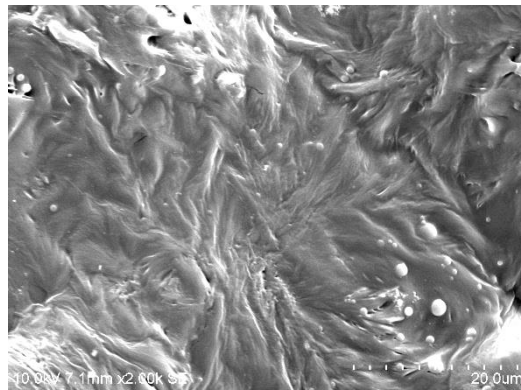


Fig. 4.22(b) SEM micrograph of PPSP-15 sample irradiated at 1×10^{11} ions/cm² fluence.

Figs. 4.22(a-d) show SEM micrographs of PPSP-15 sample before irradiation and after irradiation at three different fluences. Plasticized BPE sample shows a number of sharp pores like features which enhance with irradiation. The increased porosity upon ion irradiation suggests the formation of more polymer/liquid electrolyte interface area in the same volume of the electrolyte and a better connectivity of the liquid electrolyte through the polymer leading to higher conductivity. At higher fluence (2×10^{12} ions/cm²) the cross-linking process leads a decline in the pores.

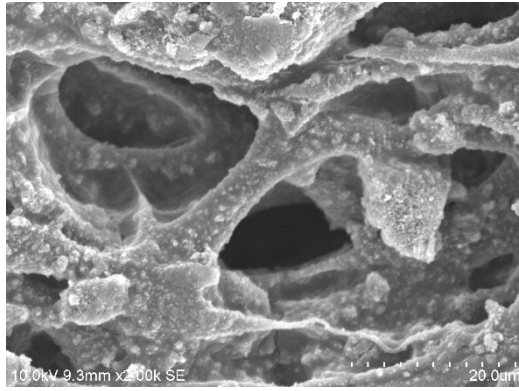


Fig. 4.22(c) SEM micrograph of PPSP-15 sample irradiated at 1×10^{12} ions/cm² fluence.

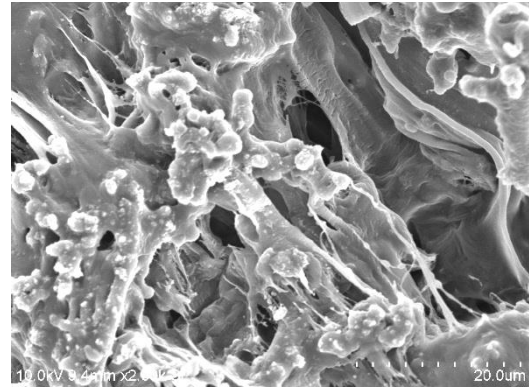


Fig. 4.22(d) SEM micrograph of PPSP-15 sample irradiated at 2×10^{12} ions/cm² fluence.

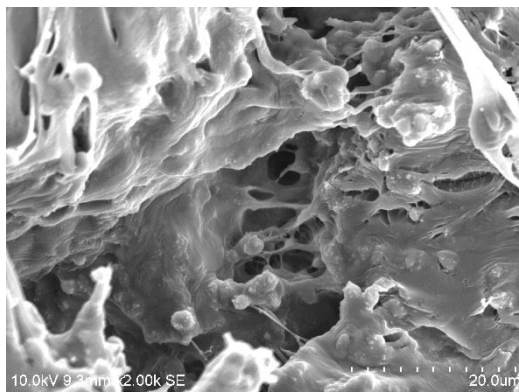


Fig. 4.23(a) SEM micrograph of un-irradiated PPSPN-12.5 sample.

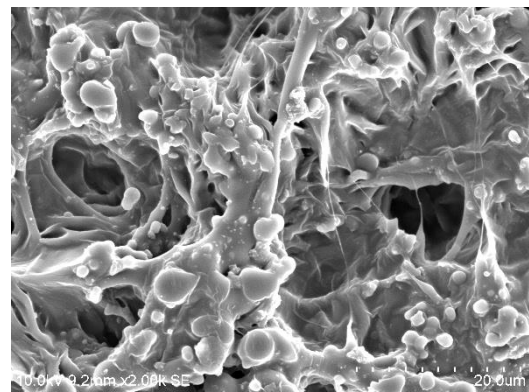


Fig. 4.23(b) SEM micrograph of PPSPN-12.5 sample irradiated at 1×10^{11} ions/cm² fluence.

EM micrographs of PPSPN-12.5 sample before irradiation and after irradiation at three different fluences are shown in **Figs. 4.23(a-d)**. Addition of SiO₂ further leads to increased number of pores structures which act as easy pathways for mobile ions to move through the matrix. Irradiation enhances the disorder in the system and consequently large number of voids are observed which serve to provide better conductivity. After the critical fluence value, cross-linking takes over and an apparent decline in the sharp features is seen.

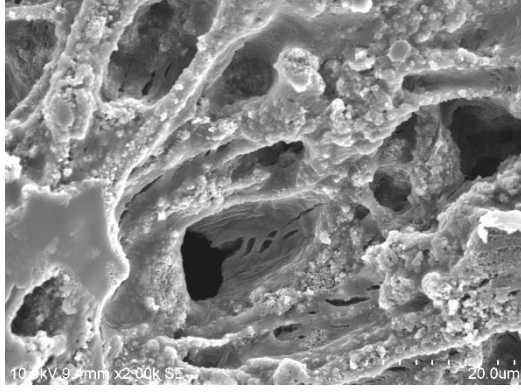


Fig. 4.23(c) SEM micrograph of PPSPN-12.5 sample irradiated at 1×10^{12} ions/cm² fluence.

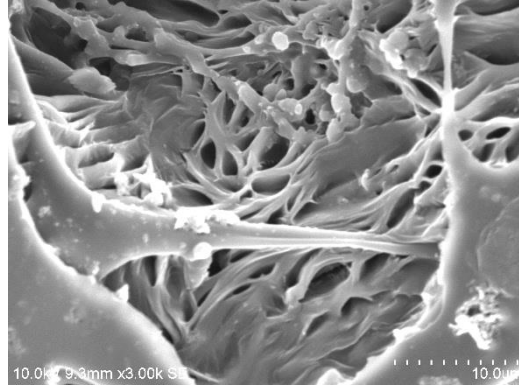


Fig. 4.23(d) SEM micrograph of PPSPN-12.5 sample irradiated at 2×10^{12} ions/cm² fluence.

A continuous change in SEM structure because of increase in disorderliness of the electrolytes, suggest an increase in amorphous nature of the system, enhancing with the increase of irradiation amount. The significant changes observed in electrolyte films confirm that irradiation by ion beam modifies the microstructure and such changes are dependent on fluence rate (*Dave and Kanchan, 2019*).

4.5 Transport Number

Transport number is one of the key factors which must be considered while selecting an electrolyte material for device application purposes. Migration of ions through the polymer matrix is the reason of electrical charge transport in polymer electrolyte systems. In such systems, total conductivity is due to the conduction of mobile ions with a negligible contribution from electrons. Transport number of ionic species in an ideal electrolyte material approaches unity with trivial electronic contribution (*Sharma, 2013*).

Conductivity of the electrolyte material (σ_i) in the form of fraction of current carried by anions, cations and electrons is measured by the transport number. The total conductivity of an electrolyte can be written as, $\sigma_T = \sigma_{e/h} + \sigma_i$ The ionic transport number is then given as $t_i = \frac{\sigma_i}{\sigma_T}$ and electronic transport number is $t_e = \frac{\sigma_e}{\sigma_T}$

Wagner's polarization technique has been adopted to measure the ion transport number in the present study. This method estimates the measure of the electronic contribution

to the total conductivity. In this method the current was monitored as a function of time on application of fixed dc potential 500 mV across the *Na//polymer electrolyte//Na* cell. The initial current measured is the total current (i_T) which is due to the ions (i_i) and the electrons (i_e). As the polarization builds up, i_e collapses and only i_i remains at last. Ionic transport number is then calculated using the equation. $t_i = \frac{\sigma_i}{\sigma_T} = \frac{i_T - i_e}{i_T}$, table 4.2 presents ion transport numbers of the prepared electrolyte samples. For PPS-system, ion transport number lies in the range from 0.80-0.91 and the ionic transport number increases monotonically with increase in salt concentration. Successive addition of the salt in the system increases the cations which are dissociated and hence highest ion transport number is recorded for PPS-17.5 sample.

Transport number values for PPSPN system are higher than PPS system and are in the range of 0.85-0.94 and show maximum value for PPSP-15 sample. Transport number increases with increase in EC+PC content up to 15 wt%. Beyond that, the number drops. Plasticizers act as the conduction pathways in between the rigid polymer matrix structure and allow better ionic mobility and it inhibits near-by polymer chain coupling and thus help in better ion transport properties. Higher amounts of EC+PC lead to cross-linking between the polymer chains and restores crystallization in the system. Increase in orderliness in the system inhibits ion motion and hence a decrease in transport number is observed at higher EC+PC content.

When the SiO₂ nano fillers are dispersed in the PPSP system, ion transport number ranges from 0.88-0.95 showing maximum for PPSPN-12.5 sample. Nano fillers are inert additives which do not interact directly with the transport process but support the ionic motion by staying put between the interstices in the polymer matrix and creating large void like structures which serve as excellent conduction pathways for the ions. Addition of SiO₂ makes it easy for the ions to move through the voids produced by it. Also, the presence of an inert nano filler reduces ion-pair interaction and thus facilitate the ion transport (*Money et al., 2012*). In case of PPSPN system, ion transport number is high for PPSPN-5 and 7.5 samples, decreases for PPSPN-10 sample, becomes maximum for PPSPN-12.5 and then again decreases slightly for PPSPN-15 sample.

From table 4.3, the polymer electrolyte samples in the present investigation show low electronic charge transport and hence it is concluded that the ion transport process is predominantly due to ionic species in the system.

Table 4.2 Ion transport number of PPS, PPSP and PPSPN samples.

Sample Code	t_i	t_e
<i>PPS-system</i>		
PPS-5	0.80	0.20
PPS-7.5	0.82	0.18
PPS-10	0.84	0.16
PPS-12.5	0.85	0.15
PPS-15	0.89	0.11
PPS-17.5	0.91	0.09
<i>PPSP-system</i>		
PPSP-5	0.85	0.15
PPSP-10	0.87	0.13
PPSP-15	0.94	0.06
PPSP-20	0.86	0.14
PPSP-25	0.87	0.13
<i>PPSPN-system</i>		
PPSPN-5	0.88	0.12
PPSPN-7.5	0.89	0.11
PPSPN-10	0.86	0.14
PPSPN-12.5	0.95	0.05
PPSPN-15	0.90	0.10

REFERENCES

1. S. Ramesh, K. H. Leen, K. Kumantha, A. K. Arof, *Spectrochimica Acta Part A: Mol. Biomol. Spectrosc.* 66 (2007) 1237–1242.
2. A. Kumar, S. Banerjee, M. Deka, (2010a.). *Electron microscopy for understanding swift heavy ion irradiation effects on electroactive polymers*. In: Mendez-Vilaz, A., Diaz, J. (Eds.), *Microscopy: Science, Technology, Applications and Education*. Formatex Research Centre, Spain, pp. 1755–1768.
3. A. Kumar, M. Deka, S. Banerjee, *Solid State Ionics*, 181 (2010b.) 609-615.
4. D. Kumar, S. A. Hashmi, *Solid State Ionics*, 181 (2010) 416-423.
5. G.P. Pandey, S.A. Hashmi, *Journal of Power Sources*, 187 (2009) 627-634.
6. S. Ketabi, K. Lian, *Electrochimica Acta*, 103 (2013) 174– 178.
7. P. Sharma, *Study of Conduction Mechanism in PEO-PMMA Polymer Blend Nano-composite Electrolytes*, Gujarat, India (2013).
8. G. Dave, D. K. Kanchan, *Indian Journal of Pure and Applied Physics*, 56 (2018) 978-988.
9. P. Pradeepa, S. Edwinraj S, P. M. Ramesh, *Chinese Chemical Letters*, 26 (2015) 1191.
10. R. Percolla, L. Calcagno, G. Foti, G. Ciavola, *Applied Physics Letters* 65 (23) (1994) 2966.
11. K. Anbazhakan, S. Selvasekarapandiyam, S. Monisha, M. Premalatha, A. Neelaveni, *Ionics*, 23 (2017) 2663–2668.
12. S. Choudhary, R. J. Sengwa, *Electrochimica Acta*, 247 (2017) 924–941.
13. J. S. Moreno, M. Armand, M. B. Berman, S. G. Greenbaum, B. Scrosati, S. Panero, *Journal of Power Sources*, 248 (2014) 695-702.
14. S. Ramesh, S-C. Lu, *Journal of Molecular Structure*, 994 (2011) 403-409.
15. R. S. Borges, D.R. Miquita, G. G. Silva, *Electrochimica Acta*, 56 (2011) 4650-4656.
16. M. Armand, *Solid State Ionics*, 69 (1994) 309-319.
17. C. Y. Chiu, W. H. Hsu, Y. J. Yen, S. W. Kuo, F. C. Chang, *Macromolecules*, 38 (2005) 6640-6647.
18. N. Seki, T. Arai, Y. Suzuki, H. Kawakami, *Polymer*, 53 (2012) 2026-2067.
19. G. Dave, D. K. Kanchan, *Radiation Physics and Chemistry*, 161 (2019) 87–94.
20. K. Money, K. Hariharan, J. Swenson, *Solid State Ionics*, 225 (2012) 346–349.